The role of high cholesterol in age-related COVID19 lethality.

Hao Wang[1,2,3], Zixuan Yuan[1,2,3], Mahmud Arif Pavel[1,2], Robert Hobson[4,5], Scott B. Hansen[1,2,*]

[1]Department of Molecular Medicine, [2]Department of Neuroscience, [3]Skaggs Graduate School of Chemical and Biological Sciences, The Scripps Research Institute, Jupiter, Florida 33458, [4]Bruker Nano Surfaces, Fitchburg, WI, 53711, USA, [5]University of Utah, Salt Lake City, Utah, 84112, USA

*Correspondence: shansen@scripps.edu

ABSTRACT

Coronavirus disease 2019 (COVID19) is a respiratory infection caused by severe acute respiratory syndrome coronavirus 2 (SARS-CoV-2) originating in Wuhan, China in 2019. The disease is notably severe in elderly and those with underlying chronic conditions. A molecular mechanism that explains why the elderly are vulnerable and why children are resistant is largely unknown. Here we show loading cells with cholesterol from blood serum using the cholesterol transport protein apolipoprotein E (apoE) enhances the entry of pseudotyped SARS-CoV-2 and the infectivity of the virion. Super resolution imaging of the SARS-CoV-2 entry point with high cholesterol shows almost twice the total number of endocytic entry points. Cholesterol concomitantly traffics angiotensinogen converting enzyme (ACE2) to the endocytic entry site where SARS-CoV-2 presumably docks to efficiently exploit entry into the cell. Furthermore, in cells producing virus, cholesterol optimally positions furin for priming SARS-CoV-2, producing a more infectious virion with improved binding to the ACE2 receptor. *In vivo*, age and high fat diet induces cholesterol loading by up to 40% and trafficking of ACE2 to endocytic entry sites in lung tissue from mice. We propose a component of COVID19 severity based on tissue cholesterol level and the sensitivity of ACE2 and furin to cholesterol. Molecules that reduce cholesterol or disrupt ACE2 localization with viral entry points or furin localization in the producer cells, may reduce the severity of COVID19 in obese patients.

INTRODUCTION

In early 2020, COVID19 spread rapidly throughout the developed world leading to extensive death and an ongoing pandemic. The lethality of SARS-CoV-2 is notably selective for elderly[1,2] and those with chronic disease such as hypertension, diabetes, Alzheimer's, cardiovascular disease, and smoking[3,4]. Interestingly, almost all children are either asymptomatic or present with very minor symptoms, while elderly and those with underlying conditions experience very severe life-threatening symptoms. This disparity was also observed with SARS-CoV, a closely related virus which failed to kill any children under the age of 12, despite being much more lethal than SARS-CoV-2 in adults[5]. Understanding why young people are resistant in this class of viruses could help both healthy and chronically ill adults to avoid severe symptoms of COVID19.

Cholesterol is an insoluble eukaryotic lipid found in membranes throughout the human body, most notably in the plasma membrane[6]. It appears to accumulate in tissue with age[7–9]. Furthermore, chronic inflammation causes cholesterol loading into macrophage rich tissue[10]. Pneumocytes in the lung load and unload cholesterol along with macrophages and this process is associated with lung disease[11] and lung function[12,13]. For further discussion on cholesterol in peripheral tissue see Figure S1B.

We recently showed a cholesterol-dependent mechanism for anesthetics that regulates the translocation of membrane proteins between monosialotetrahexosylganglioside1 (GM1) containing lipid rafts and PIP_2 lipid clusters[14,15]. Lipid rafts (see Supplemental Figure S1A) facilitate endocytosis, an important entry pathway for SARS-CoV, a closely related virus to SARS-CoV-2[16,17]. SARS-CoV-2 enters the cell by binding to a receptor angiotensinogen converting enzyme 2 (ACE2)[18,19]. Similar to the proteins in anesthesia, previous experiments showed ACE2 can associate with detergent resistant membranes (DRMs)[20,21] which are similar in composition to GM1 lipid domains. However, it is not known if this sensitivity of ACE2 to cholesterol contributes to differences in viral infectivity in young vs. old or those with pre-

existing conditions (e.g. obesity). Here we show that lung cholesterol increases in aged diabetic mice resulting in ACE2 trafficking to GM1 lipid rafts and mediating efficient viral entry.

RESULTS

Cholesterol dependent SARS-CoV-2 pseudovirus entry.

To test the cholesterol dependence of SARS-CoV-2 on viral entry we loaded cholesterol into HEK293T cells with apolipoprotein E (apoE) and blood serum and treated the cells with retrovirus pseudotyped with the SARS-CoV-2 S protein (SARS2-PV)[22,23]. A segment of the S protein binds to the ACE2 and recapitulates viral entry. ApoE is a cholesterol carrier protein linked to Alzheimer's and the severity of COVID19[24]. In tissue, apoE binds to low-density lipoprotein (LDL) receptor and facilitates loading of cholesterol into cells (Figure 1A). When apoE is in excess, it has the opposite effect; it facilitates efflux of cholesterol from the cell[25] (Supplemental Figure S1B).

We found cholesterol loading (apoE + serum) significantly increased SARS2-PV entry. Figure 1B shows viral entry increased 50% compared to control (serum only). Cholesterol unloading (apoE-serum) had the opposite effect; viral entry decreased almost 50% (Figure 1B). Methyl-beta-cyclodextrin (MβCD), a chemical known to extract cholesterol from the membrane of cells, inhibited more than 90% of SARS2-PV entry (Figure 1C). To avoid any potential effect of cholesterol directly on the virion, the cells were pretreated for all cholesterol conditions (one hour), washed and then exposed to the virion, i.e., the virion did not experience any cholesterol treatment, only the cells. To maintain consistency throughout the paper we used endogenously expressed ACE2, which is ~100 times less efficient than artificially over expressing ACE2 Supplemental Figure S2C).

VSV-G is a distantly related virus that binds the LDL receptor for entry. We found infection of cells with a pseudotyped VSV-G had much less sensitivity to cholesterol compared to SARS2-PV with identical treatment; cholesterol depletion only slightly decreased VSV-G entry (Figure 1D). Likewise, cholesterol modulation with MβCD had very little effect on VSV-G viral entry (Supplemental Figure S2A).

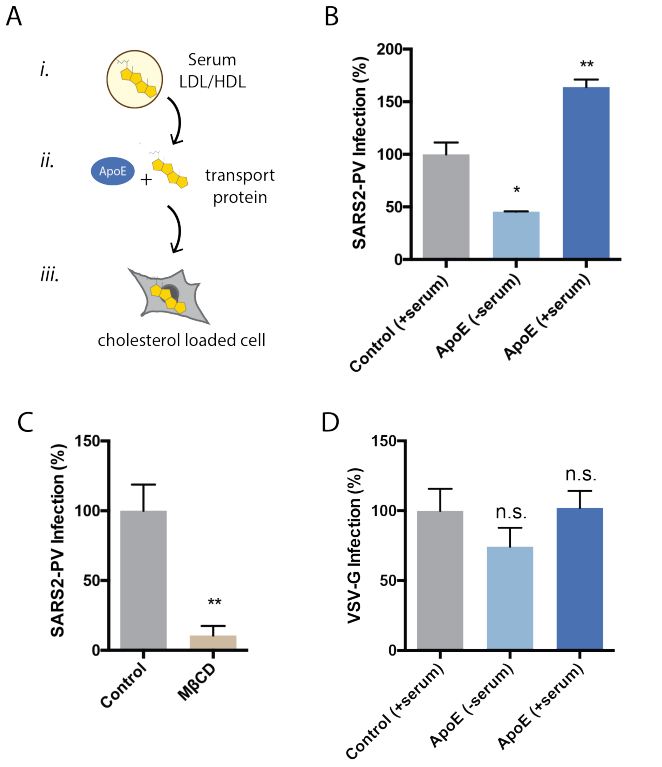

Figure 1. Cholesterol dependent inhibition of SARS-CoV-2 pseudovirus (SARS2-PV) infection (**A**) Cartoon diagram showing the experimental setup for loading cultured cells with cholesterol. ***i.***, Cholesterol (yellow shading) loaded into lipoprotein (e.g., low- and high-density lipoprotein (LDL and HDL respectively)) from blood serum. ***ii.***, Cholesterol free human apolipoprotein E (apoE, brown shading) a cholesterol transport protein is exposed to cholesterol from blood serum and ***iii,*** ApoE transports cholesterol in and out of cells (grey shading) (see also Supplemental Figure S1B). (**B**) SARS-CoV-2 pseudovirus (SARS2-PV) entry assay. Cells were treated with a luciferase expressing retrovirus pseudotyped with the SARS-CoV-2 spike protein that recapitulates viral entry. Infectivity was monitored by a luciferase activity in cells treated with or without apoE. Viral infection in cells with high cholesterol (apoE + serum) was more than 3-fold higher compared to low cholesterol. Data are expressed as mean ± s.e.m., *P<0.05, **P<0.01, one-way ANOVA. (**C**) Depletion of cellular cholesterol with methyl-beta-cyclodextrin (MβCD) blocked almost all viral entry measured by pseudotyped luciferase assay. Data are expressed as mean ± s.e.m., **P<0.01, two-sided Student's t-test. (**D**) Pseudotyped control virus, vesicular stomatitis G virus (VSV-G), is not cholesterol dependent. Data are expressed as mean ± s.e.m., n.s. P≥0.05, one-way ANOVA, n=6.

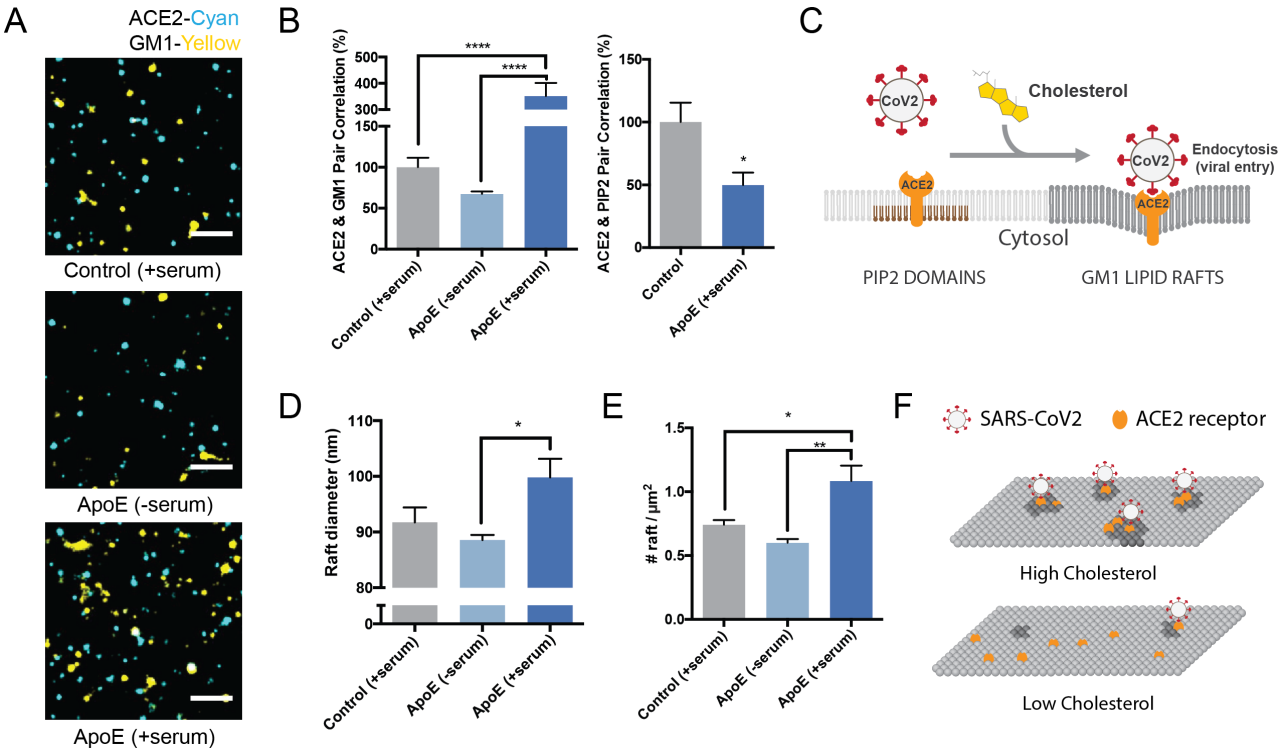

Figure 2. Molecular basis for cholesterol dependent SARS-CoV-2 entry. (**A**) Representative images from dSTORM super resolution imaging. GM1 lipid raft (yellow) increase dramatically in the presence of blood serum when apoE is present (bottom panel), labelled with CTxB. ACE2 receptor (cyan) labeled with ACE2 antibody has very little overlap with GM1 lipid rafts when blood serum is removed (middle panel). Scale bar, 1 µm. (**B**) Pair correlation from dSTORM imaging. ACE2 was compared to GM1 lipids (CTxB labeled, left) and phosphatidyl inositol 4,5-bisphosphate (PIP_2, right). Loading cells with cholesterol (apoE + serum; dark blue shading) increased the pair correlation with dependent trafficking of ACE2 in and out of lipid rafts. ApoE-mediated cholesterol influx translocates ACE2 from disordered regions into lipid rafts while. (**C**) Model showing cholesterol-dependent raft associated membrane protein translocation of ACE2 from PIP_2 domains (brown lipids) to endocytic GM1 lipids (dark grey) and enhanced SARS-CoV-2 viral entry. (**D**) Raft size analysis suggests raft assembly is regulated by apoE mediated cholesterol transportation between serum and cell membrane. (**E**) ApoE transportation of cholesterol regulates apparent raft density. Cholesterol influx from serum results in an increase in number and apparent size. Data are expressed as mean ± s.e.m., *P<0.05, **P<0.01, ***P<0.001, ****P<0.0001, one-way ANOVA.) (**F**) Model for SARS-CoV-2 viral entry in high and low cholesterol. When cholesterol is high ACE2 translocated to GM1 lipid rafts a position optimal for for viral binding and endocytosis. When cholesterol is low, ACE2 traffics away from GM1 lipid rafts and position that poorly facilitates viral infection (PIP_2 domains not shown).

Cholesterol dependent trafficking of the ACE2 receptor to endocytic entry point.

In biological membranes we have shown select raft associated proteins easily move in and out of GM1 lipids with changing cellular cholesterol levels (e.g. PLD2 and amyloid precursor protein), while other proteins remain in GM1 lipid rafts (e.g. beta and gamma secretase)[14,15,26]. Given the sensitivity of SARS2-PV to cholesterol, we hypothesized that the ACE2 receptor may likewise easily shift out of the viral entry pathway in low cholesterol.

To determine the amount of ACE2 positioned for endocytic viral entry and its sensitivity to cholesterol, we co-labeled ACE2 and GM1 lipid rafts in HEK293T cells with ACE2 antibody labelled with Cy3b and Alexa Fluor 647 conjugated fluorescent CTxB (a GM1 specific toxin), treated cells with apoE/serum, and imaged with super-resolution direct stochastical optical reconstruction microscopy (dSTORM). dSTORM and other super resolution techniques are capable of visualizing nanoscale arrangements (i.e. sub-100 nm diameter lipid domain structures) in intact cellular membranes[27–29].

Figure 2A shows representative dSTORM images of ACE2 and GM1 lipid rafts from apoE treated cells with and without serum exposure (i.e., cells loaded or not loaded with cholesterol, respectively). The association of ACE2 with GM1 lipid rafts was measured by pairwise correlation. Pairwise correlation measures the probability that two molecules are next to each other. For our experiments we compared the pair correlation at the closest radii (0-5 nm) as a percentage of control cells without apoE.

We found pairwise correlation of ACE2 with GM1 lipid rafts increased more than 3-fold in cholesterol loaded cells (Figure 2B). We loaded cholesterol using 4 μg/mL apoE and 10% serum, the same as our viral entry assay. The increased correlation was not due to a change in ACE2 concentration on the cell surface (Supplemental Figure S3A-B). As a positive control, and to confirm the effect depends on cholesterol and not another component of the serum or apoE regulation, we treated the cells with MβCD. In agreement with our viral entry assay, MβCD reduced ACE2 localization with GM1 lipid rafts by ~70% (Supplemental Figure S3C).

We then co-labeled ACE2 with an antibody that binds phosphatidylinositol 4,5-bisphate (PIP_2) lipids. PIP_2 is a polyunsaturated signaling lipid that forms domains in the disordered regions away from GM1 lipid rafts [15,30–32] (See supplemental Figure S1A). As expected, PIP_2 pair correlation was opposite of GM1, loading cells with cholesterol decreased the association of PIP_2 and ACE2 (Figure 2B). These data suggest that cholesterol traffics ACE2 from the disordered regions with PIP_2 to GM1 lipid rafts where it is positioned for endocytic viral entry (Figure 2C).

We next investigated the effect cholesterol has on the number of GM1 lipid rafts in the plasma membrane (i.e., the number of viral entry points for ACE2). Using cluster analysis, we found cells loaded with cholesterol (+apoE) increased in both the number and apparent diameter of GM1 labeled rafts compared to serum only (not loaded control) (Figure 2D-E). Cholesterol depletion by MβCD also robustly decrease the apparent raft size (Figure S3D). These decreases caused lipid rafts to separate from each other measured by Ripley's H function. (Figure S3E). The cells were fixed prior to labeling to reduce potential artifacts in their diameter size due to CTxB clustering[33] (see methods).

Cholesterol loading into lung tissue.

For cholesterol to have an effect *in vivo*, the cholesterol must be loaded into the lungs where the ACE2 expressing cells are located during an infection. To confirm age-dependent loading of cholesterol into lung tissue *in vivo*, we measured cholesterol levels in young (8-week-old) and aged (28-week-old) C57BL/6J wild type mice. Lungs were fixed, removed, and 2.5 mg of lung tissue assayed. We found cholesterol in the lung of older adults was elevated (~45%) compared to young mice (Figure 3A). The increase was significant with a P value less than 0.01.

Next we investigated the loading of cholesterol into lung tissue in aged (28 week) diabetic animals. We increased cholesterol by diet induced obesity (DIO), a well-established mouse model for type II diabetes in of C57B/6J mice [34]. We noted the weight of the obese lung was increased compared to healthy lung (Supplemental Figure S2B), most likely due to increased fluid permeability in the diabetic mouse. To control for potential excess water in the diabetic mice, we normalized the amount of cholesterol to total protein in the tissue homogenate. Cholesterol normalized per μg of protein was significantly elevated in DIO mice compared to both 8 week and 28-week-old healthy mice (40% and 22% respectively). This level of cholesterol loading is consistent with cholesterol loading into cultured cells and suggests an age and obesity induced sensitivity to viral infection exists *in vivo*.

To further confirm a cholesterol dependent effect, we tested ACE2 localization to lipid rafts in whole lung slices from obese mice. The percent pair correlation for 28wo was more than an order of magnitude higher in lungs from obese mice albeit highly variable (N=10). Nonetheless the trend was consistently higher than either young or control untreated mice (Figure 3C). Labeling in lung was sparser than in our tissue culture (Figure 3E), which likely contributing to the variability. Figure 3F shows an ACE2 based model for age and disease related SARS2 infectivity. In aged obese mice,

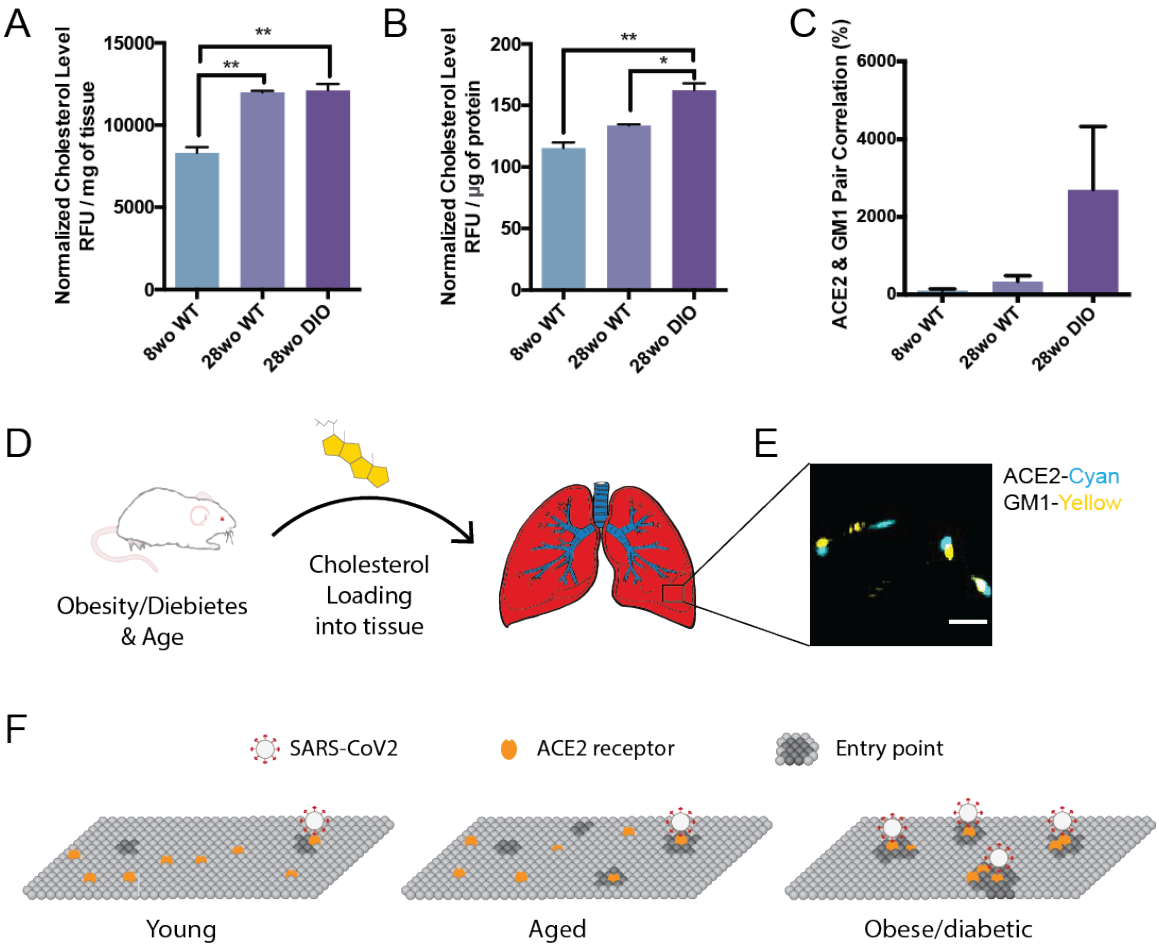

Figure 3. Age and disease dependent cholesterol loading into mouse lung. (**A-B**) Cholesterol measured per mg of lung tissue (A) and per µg of total proteins in the lung (B) in 8-week-old (wo), 28wo mice. An aged diabetic mouse, generated by diet induced obesity (DIO), loaded ~45% more cholesterol into its lung tissue per µg of total proteins. Expressed as mean ± s.e.m., *P<0.05, **P<0.01, one-way ANOVA. (**C**) Association of ACE2 with GM1 lipid rafts determined by dSTORM pair correlation in mouse lung tissue. (**D**) Cholesterol is taken up into the lung tissue of mice fed a high fat diet. (**E**) Representative dSTORM images from (C). Cholesterol (yellow shading) was loaded into the lung of mice (left) and fixed and removed and the tissue directly imaged. Scale bar, 500 nm. (**F**) Proposed model for SARS-CoV-2 infection of lung tissue of obese patients. In young, cholesterol is low, there are few entry points, and ACE2 is ill positioned with PIP_2 domains (not shown) away from GM1 lipid rafts (dark grey, entry points). With age, average cholesterol levels in the tissue increases. In obese/diabetic patients, tissue cholesterol levels are the highest and ACE2 receptor is positioned in GM1 lipid rafts for optimal viral entry (PIP_2 domains not shown).

ACE2 shifts to the GM1 lipid rafts and facilitates viral entry.

Cholesterol dependent furin localization.

In order for the virus to enter the cell, it must be primed by proteases[16]. In SARS-CoV-2 there is an efficient furin cleavage site between the S1 and S2 segments that is not found in SARS-CoV[35,36]. This S1/S2 site primes the virus for entry. During the preparation of pseudovirus, this site appears to be mostly cut in the producing cells[19,36]. For the virus to interact with a protease it must be in proximity (i.e., the same lipid compartment).

Palmitoylation is a post translation modification that attaches a 16 carbon saturated lipid to many proteins and traffics them to GM1 lipid rafts[37]. Palmitoylation of the cysteine-rich endodomain of the SARS-CoV spike glycoprotein is important

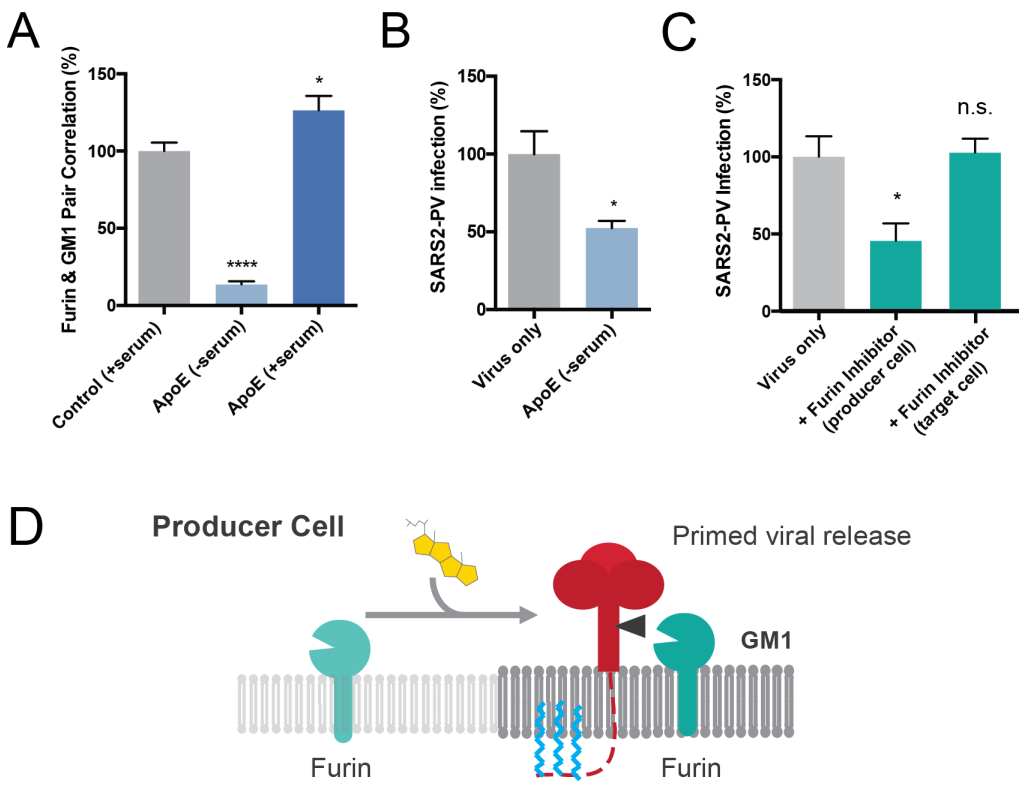

Figure 4. Assembly of viral entrance factors in GM1 lipid rafts. (**A**) Furin localization to GM1 lipid rafts is choelsterol dependent. Furin moves out of the raft under low cholesterol condition (apoE extracts cholesterol from membrane). Cholesterol loading by apoE causes an increased furin GM1 lipid pair correlation. Data are expressed as mean ± s.e.m.,*P<0.05, ****P<0.0001, one-way ANOVA. (**B**) Cholesterol depletion with apoE in producer cells decreases the efficiency of viral entry by 50%, suggesting furin's raft association is important for spike protein cleavage. Data are expressed as mean ± s.e.m., *P<0.05, two-sided Student's t-test. (**C**) Furin inhibitor blocks S1/S2 cleavage and virion priming during SARS2-PV exit from producer cells, thus decreasing the efficiency for viral entry. Furin inhibitor treatment in target cells has no effect on viral entry, however when the virus is produced in the presence of a furin inhibitor, infection decreases 50%. The result suggests furin cleavage during virus production increases SARS-CoV-2 viral entry. Data are expressed as mean ± s.e.m., *P<0.05, n.s. P≥0.05, one-way ANOVA. (**D**) Speculative role of palmitoylation in SARS-CoV-2 priming of the spike protein. In high cholesterol furin moves from the disordered lipids (light grey lipids) to ordered GM1 lipids (GM1, dark grey lipids). Cholesterol dependent membrane protein translocation is indicated by a grey arrow and the input of cholesterol (yellow shading).

for spike-mediated cell fusion and viral entry[38,39]. Little is known about palmitoylation of SARS-CoV-2. We aligned SARS-CoV and SARS-CoV-2 and found that all 9 putative palmitoylation sites in SARS-CoV are conserved in SARS-CoV-2 (Figure S4A). A single significant mutation (alanine to cysteine) introduces an additional putative palmitoylation site in SARS-CoV-2, which suggest SARS-CoV-2 remains under evolutionary pressure for palmitate driven viral infectivity.

In a virus producing cell, SARS-CoV-2 palmitoylation is positioned on the intracellular leaflet suitable for targeting the nascent spike protein to GM1 lipid rafts. To test a potential role of cholesterol in SARS-CoV-2 priming we loaded producing cells (HEK293T) with cholesterol and imaged furin trafficking in and out of lipid rafts. Cholesterol (apoE + serum) increased furin's pair correlation with GM1 lipid rafts, a location that likely favors hydrolysis of the spike protein at the S1/S2 site and facilitates priming of the virus. Unloading cholesterol from the cells (apoE - serum or MβCD) dramatically decreased the percent of furin associated with GM1 lipid rafts (Figure 4A and Supplemental Figure S4B).

A lack of furin priming has been shown to decrease viral entry[36]. If furin priming is

decreased with low cholesterol, we expect virion from low cholesterol to also produce less infectious virion. We expressed SARS2-PV in low cholesterol cells pretreated with 4 μg/ml apoE. Figure 4B shows depletion of cholesterol in producer cells yields a much weaker virion. Viral entry into normal control target cells decreased by 50%, suggesting low cholesterol likely decreases priming of the virions.

To confirm reduced cholesterol is similar to inhibited furin in our assay, we produced SARS2-PV in the presence of a furin specific inhibitor and tested viral entry. Entry was reduced ~ 50% for unprimed virus, consistent with previous results and our hypothesis (Figure 4C). Adding the inhibitor in the target cell, after the virus is already primed, had no effect (Figure 4C and Supplemental Figure S4C), suggesting furin does not cut an unprimed virion in the target cell.

Figure 4D shows a proposed model for enhanced viral entry in old compared to young due to increased S1/S2 priming in virus producing cells. In young individuals the furin is trafficked outside of GM1 lipid rafts resulting in decreased access of the spike protein to furin. In high cholesterol, furin translocates into GM1 lipid rafts near virus. Low cholesterol in the virion envelope may also contribute to the low infectivity and or recycling of furin into the Golgi (not shown).

Cholesterol dependent SARS-CoV-2 receptor binding

The effectiveness of viral entry in the disordered region could also result from reduced binding to the ACE2 in the disordered region. To test SARS-CoV-2 binding, we applied the SARS-CoV-2 receptor binding domain (RBD) to HEK293T cells with and without MβCD. MβCD treatment reduced the binding of the RBD (Supplemental Figure S4D), suggesting the virus may have evolved to bind tighter to GM1 localized ACE2. However, the effect was modest and suggests viral entry rather than binding is likely more affected by cholesterol.

DISCUSSION

Taken together our findings show the level of cellular cholesterol is a core contributor to SARS-CoV-2 viral entry. During inflammation cellular cholesterol is further increased by cytokines[10]. This suggest a unique effect where cholesterol concomitantly increases both inflammation and the efficiency of viral entry. Almost all respiratory viruses induce inflammation, but our mechanism suggests SARS-CoV-2 is particularly sensitive due to the increased entry in high cholesterol.

Based on the finding of ACE2 sensitivity to cholesterol and PIP_2 and increased cholesterol with age and disease, we propose a model for age dependent infection of SARS-CoV-2 (Figure 3F). When cholesterol is low there are very few entry points (similar to children). With age, average cellular cholesterol levels in the lung increases, thereby increasing the number and size of viral entry points (similar to adults). In chronically ill patients, cellular cholesterol levels increase dramatically and all the ACE2 receptor is positioned for viral infectivity (adults + chronic inflammation). The model is supported by age dependent loading of cholesterol into lung tissue of mice Figure 3A-B and the simultaneous translocation of ACE2 from PIP2 domains to GM1 rafts (Figure 2C).

We conclude that SARS-CoV-2 has at least three cholesterol-dependent mechanisms that likely contribute to differential infectivity in elderly with an underlying condition and with chronic inflammation. One, number of entry sites are cholesterol dependent (Figure 2E). If there are fewer endocytic points, the virus cannot enter the cell as efficiently (Figure 1B-C). Two, the cholesterol-dependent ability of the receptor, and presumably the virus, to dock into the endocytic lipids is logically one of the most important steps to infectivity. If the virus isn't positioned in the membrane correctly it likely cannot enter the cell as efficiently (Figure 1B). Third, furin priming that activates SARS-CoV-2 for membrane insertion is also sensitive to cholesterol and likely protects against severe COVID19 symptoms in low cholesterol (Figure 4D).

Our model suggests high cellular cholesterol is indicative of SARS-CoV-2 infectivity, not necessarily the levels of cholesterol in the blood. Most clinical diagnosis of cholesterol are done by analyzing blood samples, however these levels do not necessary indicate the level of cholesterol in the cellular membranes of tissue. This difference is

particularly true of chronic inflammation where blood cholesterol is low due to inhibition of cholesterol efflux proteins in the peripheral tissue[10] (see also supplementary material). Our model is consistent with a clinical study in China that showed LDL and HDL cholesterol were low in severe COVID19 patients, yet monocytes in the blood had high cholesterol[40]. The high cholesterol in monocytes is consistent with cholesterol loading into tissue during chronic inflammation.

The role of palmitoylation aiding SARS-CoV-2 priming is based on the known affinity of palmitate for GM1 ordered lipids[37] and appropriately situated spike protein for cutting in a GM1 lipid raft. However, the high cholesterol could also cause furin to be endocytosed and cycled back through the Golgi where it would interact with the spike protein as it traffics to the surface of the cell. More research is needed to understand the role of palmitoylation in SARS-CoV-2 life cycle.

Previous studies used detergent resistant membranes (DRMs) to characterize localization of ACE2 and found ACE2 association with both disordered[41,42] and ordered lipids[20]. This is consistent with our super resolution imaging in intact membranes, suggesting the DRMs are a good approximation of raft associated signal transduction. Nonetheless, super resolution imaging is an important validation of DRMs since the detergent used to prepare the DRM's may biases proteins to the disordered region.

ACE2 association with PIP_2 lipid domains is very similar to our previous finding with phospholipase D2. PIP_2 opposes the function of GM1 lipid rafts by opposing protein localization[15,43]. These results suggest that cholesterol is likely in balance with PIP_2 in the membrane to regulate the trafficking of an ACE2 in or out of the lipid raft and this may change over with age and disease.

According to our model, drugs that disrupt GM1 lipid rafts, or drugs that increase cholesterol efflux, are likely to help critically ill COVID19 patients. We and others have shown that polyunsaturated fatty acids, anesthetics, and mechanical force oppose cholesterol signaling through GM1 lipid rafts[14,15,43,44]. Drugs that inhibit cholesterol synthesis, including statins, could also be helpful, especially if taken over time to avoid early infectivity.

METHODS

Cell culture

Human embryonic kidney 293T (HEK293T) cells and HEK293T cells overexpressing human ACE2 (hACE2) were grown in Dulbecco's Modified Eagle Medium (DMEM) containing 10% fetal bovine serum (FBS) and 1% penicillin/streptomycin. HEK293T cells overexpressing hACE2 were generously provided by Dr. Michael Farzan (Department of Immunology and Microbiology, Scripps Research). Cells were generated by transduction with murine leukemia virus (MLV) pseudotyped with the vesicular stomatitis virus G protein and expressing myc-hACE2-c9, as previously described[56]. Briefly, HEK293T cells were co-transfected by PEI with three plasmids, pMLV-gag-pol, pCAGGS-VSV-G and pQCXIP-myc-hACE2-c9 at a ratio of 3:2:1, and medium was refreshed after overnight incubation of transfection mix. The supernatant with produced virus was harvested 72-hours post transfection and clarified by passing through 0.45μm filter. 293T-hACE2 cells were selected and maintained with medium containing puromycin (Sigma). hACE2 expression was confirmed by SARS2-PV entry assays and by immunofluorescence staining using mouse monoclonal antibody recognizing c-Myc.

Production of SARS-CoV-2 pseudoviruses

Retroviruses pseudotyped with the SARS-CoV-2 S proteins (SARS2-PV) was produced as previously described[22,23] with modest modifications as described. HEK293T cells were transfected by X-tremeGENE™ 9 DNA Transfection Reagent (Millipore Sigma, #6365787001) at a ratio of 5:5:1 with a plasmid encoding murine leukemia virus (MLV) gag/pol proteins, a retroviral vector pQCXIX expressing firefly luciferase, and a plasmid expressing the spike protein of SARS-CoV-2 (GenBank YP_009724390) or a control plasmid (VSV-G). All the viral plasmids were provided by Dr. Michael Farzan. Cell culture supernatant containing pseudoviruses was harvested at 72 hours post transfection. For furin inhibitor or apoE treatment, cells were incubated with 25 μM hexa-D-arginine amide (Furin Inhibitor II, Sigma-Aldrich, # SCP0148) or 4 μg/mL apoE (BioVision, #4696-

500) respectively, over the process of viral production starting 6 hours after transfection. Virus were then buffer exchanged with Amicon Ultra-4 Centrifugal Unit (Millipore Sigma, #UFC800396) to get rid of furin inhibitor in the media.

Viral entry assay

HEK293T cells were cultured in 96-well flat culture plates with transparent-bottom (Corning™ Costar™, #3585) pre-coated with poly-D-lysine. Cells were incubated with media containing 4 µg/mL apoE with or without FBS supplementation overnight before viral exposure. For MβCD treatment, cells were incubated with 100 µM MβCD for 30 min prior to virus infection. For furin inhibitor treatment, cells were incubated with 25 µM hexa-D-arginine amide for 1 hour prior to and during the whole process of virus infection.

SARS-CoV-2 pseudoviruses were applied to the cells and allowed to infect at 37 °C for 24 hours. After viral infection, efficiency of viral entry was determined through a firefly luciferase assay. Specifically, cells were washed with PBS once and 16 µL Cell Culture Lysis Reagent (Promega, #E153A) were added into each well. The plate was incubated for 15 min with rocking at room temperature. 8 µL of cell lysate from each well was added into a 384-well plate (Corning™, #3574), followed by the addition of 16 µL of Luciferase Assay Substrate (Promega, #E151A). Luciferase activity measurement was performed on a Spark 20M multimode microplate reader (Tecan). All the infection experiments were performed in a biosafety level-2 (BSL-2) laboratory.

dSTORM super-resolution imaging

Fixed cell preparation

Cells were grown to 60% confluence. Cells were incubated with 4 µg/mL purified apoE protein with or without FBS supplementation (overnight) or 100µM MβCD (30 min) in media. Cells were rinsed with PBS and then fixed with 3% paraformaldehyde and 0.1% glutaraldehyde for 20 min to fix both proteins and lipids. Fixative chemicals were reduced by incubating with 0.1% $NaBH_4$ for 7 min with shaking followed by three times 10 min washes with PBS. Cells were permeabilized with 0.2% Triton X-100 for 15 min and then blocked with a standard blocking buffer (10% bovine serum albumin (BSA) / 0.05% Triton in PBS) for 90 min at room temperature. For labelling, cells were incubated with primary antibody (anti-ACE2 antibody (Abcam, #ab189168), anti-Furin antibody (Abcam, #ab3467) or anti-TMPRSS2 antibody [EPR3861] (Abcam, #ab92323)) for 60 min in 5% BSA / 0.05% Triton / PBS at room temperature followed by 5 washes with 1% BSA / 0.05% Triton / PBS for 15 min each. Secondary antibody (donkey anti-rabbit cy3b and CTxB-647) was added in the same buffer as primary for 30 min at room temperature followed by 5 washes as stated above. Cells were then washed with PBS for 5 min. Cell labelling and washing steps were performed while shaking. Labeled cells were then post-fixed with fixing solution, as above, for 10 min without shaking followed by three 5 min washes with PBS and two 3 min washes with deionized distilled water.

Lung tissue preparation

Lungs were removed from C57BL/6J wild type and diet induced obesity (DIO) mice. Housing, animal care and experimental procedures were consistent with the Guide for the Care and Use of Laboratory Animals and approved by the Institutional Animal Care and Use Committee of the Scripps Research Institute. Mouse lung tissue slicing and staining were performed as previously described[77] with minor modifications. Mouse tissues were fixed in 4% paraformaldehyde / 1% glutaraldehyde at 4 °C for 3 days. Tissues were sliced by the histology core. Sections (50 µm) were collected and placed into 24-well plate wells containing PBS. Fixative chemicals were reduced by incubating with 0.1% $NaBH_4$ for 30 min while gently shaking at room temperature followed by three times 10 min washes with PBS. Samples were permeabilized with 0.2% Triton X-100 for 2 hours and then blocked with a standard blocking buffer (10% bovine serum albumin (BSA) / 0.05% Triton in PBS) for 6 hours at room temperature. For labelling, samples were incubated with primary antibody for 3 hours in 5% BSA / 0.05% Triton / PBS at room temperature then 3 days at 4 °C followed by 5 washes with 1% BSA / 0.05% Triton / PBS for 1 hour each. Secondary antibody was added in the same buffer as primary for 3 days at 4 °C followed by 5 washes as stated above. Sample labelling and washing steps were performed while shaking. Labeled lung tissues were then post-fixed with fixing solution, as above, for 1 hour without shaking followed by three 30 min washes with PBS and two 30 min washes with

deionized distilled water. Lung slices were mounted onto the 35 mm glass bottom chamber (ibidi, #81158) and 2% agarose were pipetted onto the slice to form a permeable agarose pad and prevent sample movement during imaging.

dSTORM imaging

Images were recorded with a Zeiss ELYRA PS.1 microscope using TIRF mode equipped with a pil-immersion 63x objective. Andor iXon 897 EMCCD camera was used along with the Zen 10D software for image acquisition and processing. The TIRF mode in the dSTORM imaging provided low background high-resolution images of the membrane. A total of 10,000 frames with an exposure time of 18 ms were collected for each acquisition. Excitation of the Alexa Fluor 647 dye was achieved using 642 nm lasers and Cy3B was achieved using 561 nm lasers. Cells and brain tissues were imaged in a photo-switching buffer comprising of 1% β-mercaptoethanol (Sigma, #63689), and oxygen scavengers (glucose oxidase (Sigma, #G2133) and catalase (Sigma, #C40)) in 50mM Tris (Affymetrix, #22638100) + 10mM NaCl (Sigma, #S7653) + 10% glucose (Sigma, #G8270) at pH 8.0. Sample drift during acquisition was corrected by an autocorrelative algorithm.

For PIP2 imaging, images were recorded with a Bruker Vutara 352 with a 60X Olympus Silicone objective. Frames with an exposure time of 20 ms were collected for each acquisition. Excitation of the Alexa Fluor 647 dye was achieved using 640 nm lasers and Cy3B was achieved using 561 nm lasers. Laser power was set to provide isolated blinking of individual fluorophores. Cells were imaged in a photo-switching buffer comprising of 1% β-mercaptoethanol (Sigma-Aldrich, #63689), 50 mM cysteamine (Sigma-Aldrich #30070) and oxygen scavengers (glucose oxidase (Sigma, #G2133) and catalase (Sigma, #C40)) in 50mM Tris (Affymetrix, #22638100) + 10mM NaCl (Sigma, #S7653) + 10% glucose (Sigma, #G8270) at pH 8.0. Axial sample drift was corrected during acquisition through the Vutara 352's vFocus system.

Images were constructed using the default modules in the Zen software. Each detected event was fitted to a 2D Gaussian distribution to determine the center of each point spread function plus the localization precision. The Zen software also has many rendering options including removing localization errors and outliers based on brightness and size of fluorescent signals. Pair correlation and cluster analysis was performed using the Statistical Analysis package in the Vutara SRX software. Pair Correlation analysis is a statistical method used to determine the strength of correlation between two objects by counting the number of points of probe 2 within a certain donut-radius of each point of probe 1. This allows for localization to be determined without overlapping pixels as done in traditional diffraction-limited microscopy. Raft size estimation and raft density were calculated through cluster analysis by measuring the length and density of the clusters comprising of more than 10 particles with a maximum particle distance of 0.1 μm. Ripley's H(r) analysis was performed to study the distribution of lipid raft clusters.

Lung cholesterol assay

To measure the relative changes in cholesterol level in lung tissue, we developed an Amplex Red-based cholesterol assay. Lungs were removed from C57BL/6J wild type and diet induced obesity (DIO) mice.___Housing, animal care and experimental procedures were consistent with the Guide for the Care and Use of Laboratory Animals and approved by the Institutional Animal Care and Use Committee of the Scripps Research Institute. The left lobe of each lung was homogenized with RIPA lysis buffer. After centrifugation, supernatant was collected for cholesterol and protein measurement. 50 μL of supernatant were mixed with 50 μL of assay solution containing 100 μM Amplex red, 2 U/mL horseradish peroxidase, 4 U/mL cholesterol oxidase and 4 U/mL cholesteryl esterase in PBS in 96-well plates with transparent-bottom (Corning™ Costar™, #3585). Relative cholesterol concentration was determined for each sample by measuring fluorescence activity with a fluorescence microplate reader (Tecan Infinite 200 PRO, reading from bottom) with excitation wavelength of 530 nm and an emission wavelength of 585 nm. Subsequently, cholesterol level was normalized by tissue weights and protein concentration. Cholesterol signals were then graphed (Mean ± s.e.m.) and statistically analyzed (one-way ANOVA) with GraphPad Prism software (v6.0f).

Receptor binding domain (RBD) binding assay

HEK293T cells were seeded into 96-well flat culture plates with transparent-bottom (Corning™ Costar™, #3585) one day before experiment. SARS-CoV-2 RBD with a human Fc fusion was a generous gift from Dr. Michael Farzan (Department of Immunology and Microbiology, Scripps Research). HEK293T cells were incubated with 10 µg/mL RBD peptide in cell culture medium overnight at 37°C in 5% CO_2. Cells were washed with PBS once before fixation with 3% paraformaldehyde. After blocking with a standard blocking buffer (10% bovine serum albumin (BSA) / 0.05% Triton in PBS) for 90 min at room temperature, RBD binding to the cells were labelled with Alexa 647 goat anti-human IgG (Jackson ImmunoResearch, # 109-606-098) for 6 hours at 4°C. After labelling, cells were washed with PBS twice. Relative RBD binding was determined in quintuplicate for each condition by measuring fluorescent activity with a fluorescence microplate reader (Tecan Infinite 200 PRO) with excitation wavelength of 630 nm and an emission wavelength of 680 nm.

Statistical analyses

All statistical calculations were performed in GraphPad Prism v6.0. For the Student's t test, significance was calculated using a two-tailed unpaired parametric test with significance defined as $p < 0.05$, **P<0.01, ***P<0.001, ****P<0.0001. For the multiple comparison test, significance was calculated using an ordinary one-way ANOVA with Dunnett's multiple comparisons test.

Acknowledgements

We thank Michael Farzan for the SARS-CoV-2 spike plasmid, hACE2 overexpression HEK293T cell line, and RBD peptide; Andrew S. Hansen for helpful discussion and reading of the manuscript; Montina Van Meter from histology core and Scott Troutman from the Joseph Kissil Lab (Scripps Research, FL) for support in tissue immunohistochemistry. This work was supported by the National Institutes of Health with an R01 to S.B.H. (R01NS112534) and the US Department of Defense with an Accelerating Innovation in Military Medicine to S.B.H. (W81XWH1810782). We are grateful to the Iris and Junming Le Foundation for funds to purchase a super-resolution microscope, making this study possible.

References

1. Wu, Z. & McGoogan, J. M. Characteristics of and Important Lessons from the Coronavirus Disease 2019 (COVID-19) Outbreak in China: Summary of a Report of 72314 Cases from the Chinese Center for Disease Control and Prevention. *JAMA - J. Am. Med. Assoc.* **323**, 13–16 (2020).
2. Wu, J. T. *et al.* Estimating clinical severity of COVID-19 from the transmission dynamics in Wuhan, China. *Nat. Med.* **26**, (2020).
3. Chu, J. *et al.* Clinical Characteristics of 54 medical staff with COVID-19: A retrospective study in a single center in Wuhan, China. *J. Med. Virol.* 0–3 (2020). doi:10.1002/jmv.25793
4. Chen, T. *et al.* Clinical characteristics of 113 deceased patients with coronavirus disease 2019: retrospective study. *BMJ* **368**, m1091 (2020).
5. Stockman, L. J. *et al.* Severe acute respiratory syndrome in children. *Pediatr. Infect. Dis. J.* **26**, 68–74 (2007).
6. Dang, E. V., Madhani, H. D. & Vance, R. E. Cholesterol in quarantine. *Nat. Immunol.* **21**, 716–717 (2020).
7. Angel, A. & Farkas, J. Regulation of cholesterol storage in adipose tissue. *J. Lipid Res.* **15**, 491–499 (1974).
8. Adams, C. W., Bayliss, O. B., Baker, R. W., Abdulla, Y. H. & Hunter-Craig, C. J. Lipid deposits in ageing human arteries, tendons and fascia. *Atherosclerosis* **19**, 429–40 (1974).
9. Sene, A. *et al.* Impaired cholesterol efflux in senescent macrophages promotes age-related macular degeneration. *Cell Metab.* **17**, 549–561 (2013).
10. Tall, A. R. & Yvan-Charvet, L. Cholesterol, inflammation and innate immunity. *Nat. Rev. Immunol.* **15**, 104–116 (2015).
11. Gowdy, K. M. & Fessler, M. B. Emerging roles for cholesterol and lipoproteins in lung disease. *Pulm. Pharmacol. Ther.* **26**, 430–7 (2013).
12. Fessler, M. B. A new frontier in immunometabolism cholesterol in lung health and disease. *Ann. Am. Thorac. Soc.* **14**, S399–S405 (2017).
13. Andersson, J. M., Grey, C., Larsson, M., Ferreira, T. M. & Sparr, E. Effect of cholesterol on the molecular structure and transitions in a clinical-grade lung surfactant extract. *Proc. Natl. Acad. Sci. U. S. A.* **114**, E3592–

E3601 (2017).
14. Pavel, M. A., Petersen, E. N., Wang, H., Lerner, R. A. & Hansen, S. B. Studies on the mechanism of general anesthesia. *Proc. Natl. Acad. Sci. U. S. A.* **117**, 13757–13766 (2020).
15. Petersen, E. N., Chung, H.-W., Nayebosadri, A. & Hansen, S. B. Kinetic disruption of lipid rafts is a mechanosensor for phospholipase D. *Nat. Commun.* **7**, 13873 (2016).
16. Simmons, G., Zmora, P., Gierer, S., Heurich, A. & Pöhlmann, S. Proteolytic activation of the SARS-coronavirus spike protein: Cutting enzymes at the cutting edge of antiviral research. *Antiviral Research* **100**, 605–614 (2013).
17. Lingwood, D. & Simons, K. Lipid rafts as a membrane-organizing principle. *Science* **327**, 46–50 (2010).
18. Li, W. *et al.* Angiotensin-converting enzyme 2 is a functional receptor for the SARS coronavirus. *Nature* **426**, 450–4 (2003).
19. Hoffmann, M. *et al.* SARS-CoV-2 Cell Entry Depends on ACE2 and TMPRSS2 and Is Blocked by a Clinically Proven Protease Inhibitor. *Cell* **181**, 271-280.e8 (2020).
20. Lu, Y., Liu, D. X. & Tam, J. P. Lipid rafts are involved in SARS-CoV entry into Vero E6 cells. *Biochem. Biophys. Res. Commun.* **369**, 344–349 (2008).
21. Glende, J. *et al.* Importance of cholesterol-rich membrane microdomains in the interaction of the S protein of SARS-coronavirus with the cellular receptor angiotensin-converting enzyme 2. *Virology* **381**, 215–221 (2008).
22. Quinlan, B. D. *et al.* The SARS-CoV-2 receptor-binding domain elicits a potent neutralizing resonse without antibody-dependent enhancement. *bioRxiv* 1–9 (2020). doi:10.1101/2020.04.10.036418
23. Moore, M. J. *et al.* Retroviruses Pseudotyped with the Severe Acute Respiratory Syndrome Coronavirus Spike Protein Efficiently Infect Cells Expressing Angiotensin-Converting Enzyme 2. *J. Virol.* **78**, 10628–10635 (2004).
24. Kuo, C.-L. *et al.* APOE e4 genotype predicts severe COVID-19 in the UK Biobank community cohort. *Journals Gerontol. Ser. A* 1–29 (2020). doi:10.1093/gerona/glaa131
25. Luo, J., Yang, H. & Song, B. L. Mechanisms and regulation of cholesterol homeostasis. *Nat. Rev. Mol. Cell Biol.* **21**, 225–245 (2020).
26. Wang, H., Kulas, J. A., Ferris, H. A. & Hansen, S. B. Regulation of amyloid processing in neurons by astrocyte-derived cholesterol. *bioRxiv* 2020.06.18.159632 (2020). doi:10.1101/2020.06.18.159632
27. Betzig, E. *et al.* Imaging intracellular fluorescent proteins at nanometer resolution. *Science* **313**, 1642–1645 (2006).
28. Hess, S. T., Girirajan, T. P. K. K. & Mason, M. D. Ultra-high resolution imaging by fluorescence photoactivation localization microscopy. *Biophys. J.* **91**, 4258–4272 (2006).
29. Sahl, S. J., Hell, S. W. & Jakobs, S. Fluorescence nanoscopy in cell biology. *Nat. Rev. Mol. Cell Biol.* **18**, 685–701 (2017).
30. Wang, J. & Richards, D. a. Segregation of PIP2 and PIP3 into distinct nanoscale regions within the plasma membrane. *Biol. Open* **1**, 857–62 (2012).
31. van den Bogaart, G. *et al.* Membrane protein sequestering by ionic protein-lipid interactions. *Nature* **479**, 552–5 (2011).
32. Robinson, C. V., Rohacs, T. & Hansen, S. B. Tools for Understanding Nanoscale Lipid Regulation of Ion Channels. *Trends Biochem. Sci.* **44**, 795–806 (2019).
33. Petersen, E. N., Pavel, M. A., Wang, H. & Hansen, S. B. Disruption of palmitate-mediated localization; a shared pathway of force and anesthetic activation of TREK-1 channels. *Biochim. Biophys. Acta - Biomembr.* **1862**, 183091 (2020).
34. Wang, C.-Y. & Liao, J. K. A mouse model of diet-induced obesity and insulin resistance. *Methods Mol. Biol.* **821**, 421–33 (2012).
35. Coutard, B. *et al.* The spike glycoprotein of the new coronavirus 2019-nCoV contains a furin-like cleavage site absent in CoV of the same clade. *Antiviral Research* **176**, (2020).
36. Hoffmann, M., Kleine-Weber, H. & Pöhlmann, S. A Multibasic Cleavage Site in the Spike Protein of SARS-CoV-2 Is Essential for Infection of Human Lung Cells. *Mol. Cell* **78**, 779-784.e5 (2020).
37. Levental, I., Lingwood, D., Grzybek, M., Coskun, U. & Simons, K. Palmitoylation regulates raft affinity for the majority of integral raft proteins. *Proc. Natl. Acad. Sci.* **107**, 22050–22054 (2010).
38. Petit, C. M. *et al.* Palmitoylation of the cysteine-rich endodomain of the SARS-coronavirus spike glycoprotein is important for spike-mediated cell fusion. *Virology* **360**, 264–274 (2007).
39. McBride, C. E. & Machamer, C. E. Palmitoylation of SARS-CoV S protein is necessary for partitioning into detergent-resistant membranes and cell-cell fusion but not interaction with M protein. *Virology* **405**, 139–148 (2010).
40. Hu, X., Chen, D., Wu, L., He, G. & Ye, W. Low Serum Cholesterol Level Among Patients with COVID-19 Infection in Wenzhou, China. *SSRN Electron. J.* (2020). doi:10.2139/ssrn.3544826
41. Warner, F. J. *et al.* Angiotensin-converting enzyme 2 (ACE2), but not ACE, is preferentially localized to the apical surface of polarized kidney cells. *J. Biol. Chem.* **280**, 39353–39362 (2005).
42. Li, G. M., Li, Y. G., Yamate, M., Li, S. M. & Ikuta, K. Lipid rafts play an important role in the early stage of severe

acute respiratory syndrome-coronavirus life cycle. *Microbes Infect.* **9**, 96–102 (2007).

43. Nayebosadri, A., Petersen, E. N., Cabanos, C. & Hansen, S. B. A Membrane Thickness Sensor in TREK-1 Channels Transduces Mechanical Force. *SSRN Electron. J.* (2018). doi:10.2139/ssrn.3155650

44. Petersen, E. N. *et al.* Phospholipase D Transduces Force to TREK-1 Channels in a Biological Membrane. 758896 (2019). doi:10.1101/758896

Supplemental Figures

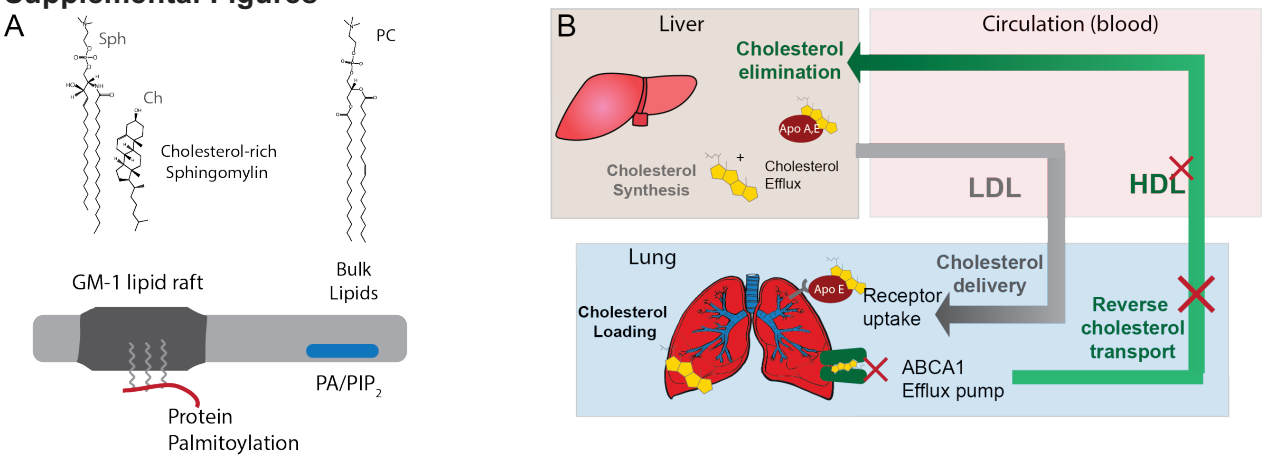

Figure S1. Cholesterol transport and function in GM1 lipid rafts (**A**) The side view of a plasma membrane is shown (top extracellular). The membrane partitions into regions of ordered (saturated) and disordered (unsaturated) lipids. The ordered region contains cholesterol and sphingolipids (Sph). Packing of cholesterol with saturated lipids is thought to provide order and makes ordered lipids thicker than disordered lipids. The disordered region contains unsaturated lipids including phosphatidylcholine (PC), phosphatidic acid (PA), and phosphatidylinositol 4,5-bisphosphate (PIP_2). PIP_2 and PA are signaling lipids and PIP_2 forms its own lipid domains separate from GM1 lipid rafts. Palmitoylation of proteins typically occurs on the cytosolic portion of the membrane and inserts into the inner leaflet (red line with lipids attached). For a virus that exits the cell the palmitoylation may insert into the extracellular leaflet. (**B**) Cartoon of cholesterol loading into lung pneumocyte's and macrophages. In healthy individuals most cholesterol is produced in the liver. Cholesterol effluxes through ATP binding cassette (ABC) transporters (not shown) and is loaded into apolipoproteins (e.g., A and E; apoA and apoE). The cholesterol is then transported through the blood serum in the form of high- and low- density lipoproteins to the lung. In the lung, receptors located on individual cell membranes (shown as one receptor for simplicity) take up the cholesterol. In healthy individuals, excess cholesterol is effluxed with ABCA1 transporter (green shading) from the plasma membrane of individual cells, loaded into apoA1 or apoE and transported back to the liver for elimination. During chronic inflammation reverse cholesterol transport is inhibited and cholesterol is loaded into macrophage rich tissues in the periphery.

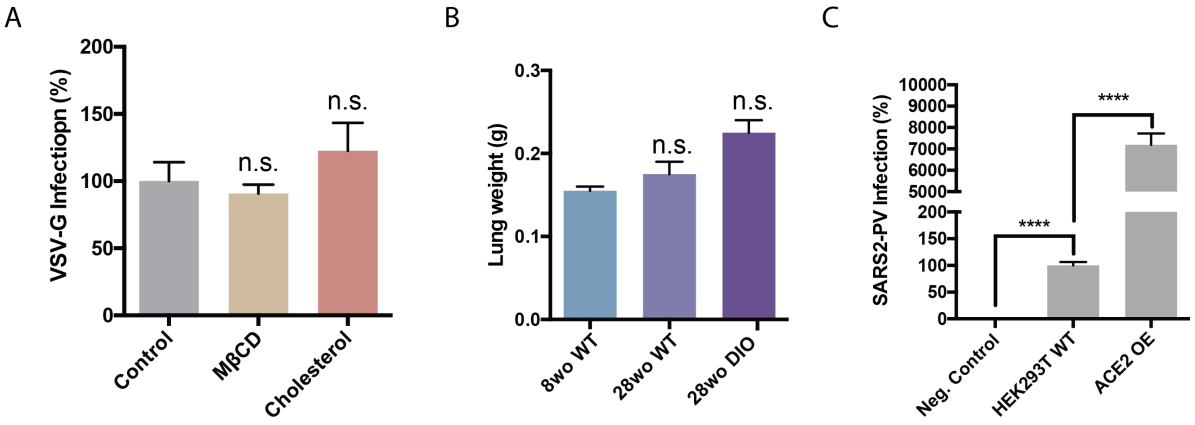

Figure S2. VSV-G viral entry and lung weight. (**A**) Cells were treated with MβCD and a luciferase expressing retrovirus pseudotyped with the VSV-G protein. VSV-G is a similar but distant virus compared to SARS-CoV-2 and serves as a control for age-dependent cholesterol selectivity. Infectivity was monitored by a luciferase activity in cells treated with methyl-beta-cyclodextrin (MβCD) or MβCD with cholesterol. Data are expressed as mean ± s.e.m., n.s.>0.05, one-way ANOVA. (**B**) Lung weight per mg of lung tissue. Lungs were extracted from 8-week-old (wo) and 28wo mice, fixed and assayed for cholesterol with a fluorescent assay. Data are expressed as mean ± s.e.m., n.s.>0.05 , one-way ANOVA. (**C**) SARS2 PV viral entry with wild type HEK293T expressing endogenous ACE2 (HEK293T WT) and HEK293T cells overexpressing hACE2 (ACE2 OE). Negative (neg.) control are HEK293T cells treated identical to the other conditions except no virus was applied. The endogenous expression was low but presumably much more physiologically relevant and shows ACE2 is expressed in HEK293T sells albeit at comparatively low quantities. The result is a single side by side comparison, but the values are in a typical range we see for these two systems. Data are expressed as mean ± s.e.m., ****P<0.0001, two-sided Student's t-test.

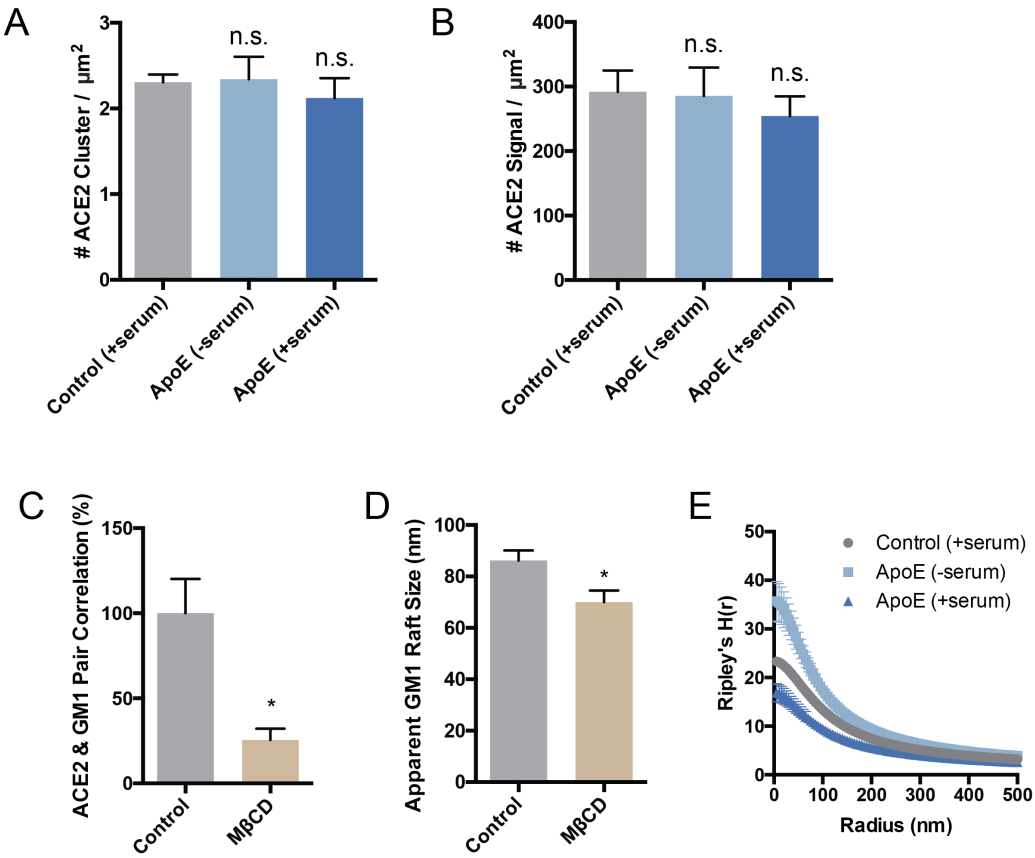

Figure S3. dSTORM of ACE2 cluster (**A**) and signal (**B**) shows that the expression of ACE2 remains roughly constant when cells are loaded or unloaded with cholesterol by the cholesterol transport protein apoE. Although, while not statistically significant ACE2 expression appears to slightly decrease in high cholesterol (ApoE + serum) which agrees with the clinical findings of decreased ACE2 surface expression in older people. Data are expressed as mean ± s.e.m.,*P<0.05, one-way ANOVA. (**C**) Cholesterol depletion with methyl-beta-cyclodextrin (MβCD) diminishes ACE2's raft localization. (**D**) Cholesterol depletion by MβCD robustly decreases the apparent size of GM1 lipid rafts after CTxB clusterin. Data are expressed as mean ± s.e.m., *P<0.05, two-sided Student's t-test. (**E**) Ripley's H-Function (H(r)) showing raft separation after cholesterol depletion while distance between rafts gets shorter as apoE transports cholesterol from serum into the membrane.

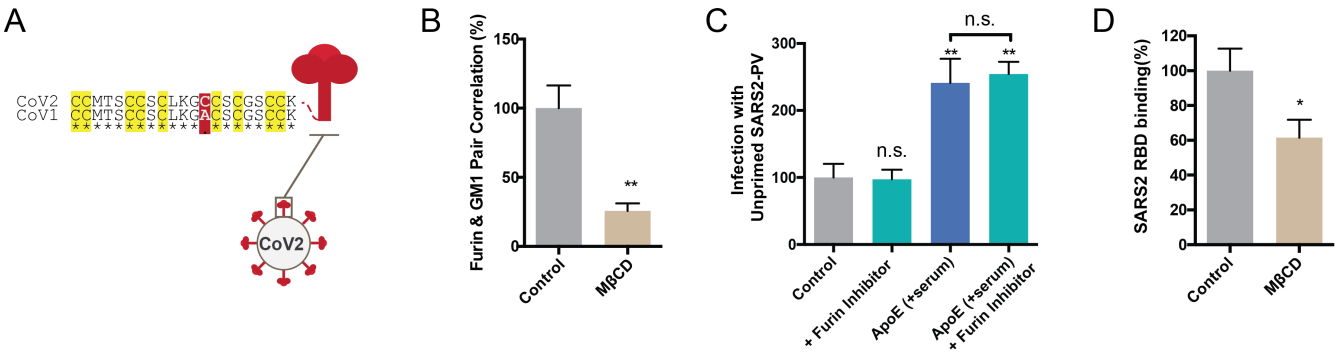

Figure S4. dSTORM of viral processing proteases. (**A**) Sequence alignment of the palmitoylation site in SARS-CoV (GenBank: ABD72995.1) and SARS-CoV-2 (GenBank: QII57161.1). Residues conserved are marked with an asterisk. All 9 putative palmitoylation sites identified in SARS-CoV are conserved in SARS-CoV-2 (yellow highlight). A single mutation introduces a 10th putative palmitoylation site (red shading). (**B**) Cholesterol depletion by MβCD traffics furin out of the GM1 lipid rafts into disordered regions. Data are expressed as mean ± s.e.m., **P<0.01, two-sided Student's t-test. (**C**) Unprimed virion was produced in HEK cells with furin inhibitor and used to infect cells with and without furin inhibitor and with and without apoE. Furin inhibitor did not change the infectivity of the unprimed virion with or with cholesterol loading (apoE). Hence, furin appears unable to cut the virion in the target cell. Data are expressed as mean ± s.e.m., **P<0.01, n.s. P≥0.05, one-way ANOVA. (**D**) The receptor binding domains (RBD) of SARS-CoV-2 was added to cells treated with or without methyl-beta-cyclodextrin (MβCD). Binding was measured by fluorescence from an Alexa 647 labeled antibody to an Fc tag on the RBD protein.